Nano Today 45 (2022) 101538

Contents lists available at ScienceDirect

Nano Today

journal homepage: www.elsevier.com/locate/nanotoday

Elucidating facet dependent electronic and electrochemical properties of Cu_2O nanocrystals using AFM/SCEM and DFT

Qingquan Ma[a], Joshua Young[b], Sagnik Basuray[b], Guangming Cheng[c], Jianan Gao[a], Nan Yao[c], Wen Zhang[a,b,*]

[a] John A. Reif, Jr. Department of Civil and Environmental Engineering, New Jersey Institute of Technology, Newark, NJ 07102, United States
[b] Otto H. York Department of Chemical and Materials Engineering, New Jersey Institute of Technology, Newark, NJ 07102, United States
[c] Princeton Institute for the Science and Technology of Materials, Princeton University, Princeton, NJ 08544, United States

ARTICLE INFO

Article history:
Received 14 April 2022
Received in revised form 2 June 2022
Accepted 20 June 2022
Available online xxxx

Keywords:
Cu_2O
Facet engineering
Electrochemical activity
AFM-SECM
KPFM
DFT

ABSTRACT

Cuprous oxide (Cu_2O) has extensively been studied owing to its excellent optical, magnetic, and catalytic properties. Many of these properties are facet-dependent and have not been well elucidated. This work synthesized cubic, cuboctahedral, octahedral, and rhombic dodecahedral shaped Cu_2O nanocrystals of ~300 nm in size to evaluate the facet-dependent electrochemical activities. Cyclic voltammetry (CV) and electrochemical impedance spectroscopy (EIS) were firstly used to reveal the average electrochemical activities at the ensemble level. Atomic force microscopy-scanning electrochemical microscopy (AFM-SECM) was further used to assess the electrochemical activities of different Cu_2O nanocrystals at the facet level. Hexaammineruthenium (III) chloride ($\{Ru(NH_3)_6\}Cl_3$) was employed as the probe molecules that reacted with four different Cu_2O nanocrystals under −400 mV and yielded ~300 pA current between the probing tip and the nanocrystal surface. The tip-current mapping results indicate that rhombic dodecahedral Cu_2O exhibits higher electrocatalytic activity than other shaped Cu_2O, due to the presence of dominant exposed facet of {110} as indicated by the relatively high tip current. Density-functional theory (DFT) calculations confirmed the facet dependence of local surface energy and electronic structure of Cu_2O nanocrystals. Besides electrochemical activity, the surface work function and adsorptive properties were both observed to vary with the shape and dominant exposed facets of Cu_2O. This study presented a unique experimental and computational chemistry approach to analyze surface electrochemical properties of Cu_2O crystals at a crystalline facet level.

Introduction

It is commonly known that the smaller nanoparticle size becomes, the larger their surface area, resulting in greater reactivity or other surface properties. However, recent studies demonstrated that a smaller size does not necessarily correlate with reactivity, suggesting that other aspects such as the exposed crystal surfaces or facets begin to govern the nanoparticle reactivity at nanoscale.[1] For instance, many metal-oxide nanoparticles such as Cu_2O and Ag_2O in cubic, cuboctahedral, octahedral, and rhombic dodecahedral shapes elicit facet-dependent catalytic, photocatalytic, and molecular adsorption properties.[2,3] For example, Amanda et al. discovered that the adsorption of selenium oxyanions onto the {110} hematite facets was higher than that of {012} using extended X-ray absorption fine edge spectroscopy (EXAFS).[4] Chen et al. demonstrated that {111} facets of Pt or Pd NPs are significantly more active than {001} facets toward carbon monoxide (CO) oxidation using diffuse reflectance infrared Fourier transform spectroscopy (DRIFTS).[5] Wu et al. reported that the water-splitting reactions on CeO_2 {110} and {111} facets are 10 ~ 100 times faster than that on CeO_2 {100} facet at temperature (T) < 950 K using DFT simulations.[6] Huang et al. reported that the band structures, electrical conductivities and photocatalytic activities of facet-specific Cu_2O cube, octahedron, and rhombic dodecahedron are highly related to their exposure facets.[7–9] For example, the {100} facet of Cu_2O has a fixed band gap of 1.787 eV, while {110} and {111} yielded an oscillating band gap between 0 and 1.787 eV. Moreover, the {111}-octahedron is highly conductive, whereas the {110}-rhombic dodecahedron is insulating and the {100} facet is moderately conductive. Finally, the photocatalytic activities of Cu_2O follow the order

---

[*] Corresponding author at: John A. Reif, Jr. Department of Civil and Environmental Engineering, New Jersey Institute of Technology, Newark, NJ 07102, United States.
E-mail address: wen.zhang@njit.edu (W. Zhang).

https://doi.org/10.1016/j.nantod.2022.101538
1748-0132/

of {110}-rhombic dodecahedron > {111}- octahedron > {100}-cube. Furthermore, control of surface termination on TiO_2 nanoparticles can enhance the electrochemical reaction selectivity and suppress the competing reaction pathways or byproduct interference.[10,11] Peng et al. examined the electronic states and structures of TiO_2 on particular facets such as {001} and {101} using ^{31}P nuclear magnetic resonance (NMR) in combination with trimethylphosphine (TMP) as a surface probe. They found that surface Ti cations on various facets with different Lewis acidities, surface energies, and steric arrangements are different.[12].

Characterizing the influences of surface crystal facets on their properties at the nanoscale or atomic scale still remains challenging, because many surface characterization techniques such as Raman mapping, electrochemical measurements, surface plasmon resonance, and fluorescence microscopy usually resolve the average information of surface properties or at the single nanoparticle level. Only a few techniques such as XAFS NMR, DRIFTS, and liquid cell (high-resolution) transmission electron microscopy (LCTEM) were demonstrated to detect facet-level material properties.[13–15] For example, Sung et al. reported the different etching redox behavior of {100} for reduction and {111} for oxidation of ceria-based nanocrystals under the control of redox-governing factors using LCTEM.[16] By contrast, traditional electrochemical measurements, such as cyclic voltammetry (CV), linear sweep voltammetry (LSV), and electrochemical impedance spectroscopy (EIS), only resolves average surface information of bulk materials or aggregated nanoparticles.[17,18] Interpretation of macroscale electrochemical measurement results may be affected by nanoparticle aggregation states or surface coverage of nanoparticles on the electrode surface. Similarly, scanning electrochemistry microscopy (SECM) employs microelectrode probes that thus achieves a micrometer resolution. For nanoscale characterization, atomic force microscopy-scanning electrochemical microscopy (AFM-SECM) has increasingly been used in simultaneously probing morphology and electrochemically active sites of various nanomaterials, such as dimensionally stable anodes,[19] noble metal nanoparticles,[20] functionalized electrodes,[21] and soft electronic devices.[22] For example, mediator-tethered AFM-SECM successfully reveals the local electrochemical activity of 20-nm gold nanoparticles/nanodots functionalized by redox-labeled PEG chains deposited on gold surface.[20] Catalytic current mapping of oxygen reduction reaction or hydrogen peroxide generation on individual 300-nm Pt particles was achieved by AFM-SECM.[23,24] Thus, the catalytic particles' surface activity under activation controlled and diffusion controlled electrochemical reaction conditions could be measured.

This study employed AFM-SECM to examine the facet/shape-dependent electrochemical properties of individual cuprous oxide (Cu_2O) nanocrystals of four shapes: nanocubes with the dominant {100} facet, rhombic dodecahedrons with the dominant {110} facet, octahedrons with the dominant {111} facet, and cuboctahedrons with {111} and {100} facets. Cu_2O is a p-type semiconductor with a direct band gap of about 2.17 eV,[25] which emerges as a promising material in photocatalysis,[26] catalysis,[27] antibacterial activity,[28] gas sensor,[29,30] supercapacitors,[31] lithium-ion batteries,[32] ion detection,[33] surface-enhanced Raman scattering (SERS),[34] organocatalysis,[35] and photoelectrochemical water splitting.[36] Here, we performed AFM-SECM mapping on cuprous oxide (Cu_2O) nanoparticles with different shapes or exposed facets. To support the facet-dependent electrochemical analysis, kelvin probe force microscopy (KPFM) was also conducted to measure the local work function of the different facets. Finally, density functional theory (DFT) simulations were performed to assess the electron transfer at the interface of different cuprous oxide (Cu_2O) nanocrystals and interpret the facet-dependent electrochemical properties.

Materials and methods

Preparation of cuprous oxide (Cu_2O) nanoparticles with different exposed facets

Copper (II) chloride dihydrate ($CuCl_2{\cdot}2H_2O$), Sodium hydroxide, Sodium dodecyl sulfate (SDS), and hydroxylamine hydrochloride ($NH_2OH{\cdot}HCl$) were purchased from Fisher Scientific. Deionized water was used to prepare all solutions which is produced from a Milli-Q water machine (Direct–Q 3UV, Millipore) that produces ultrapure deionized water with resistivity of 18.2 MΩ·cm at 25 °C. To avoid the effect of the surface-capping ligands on catalytic activities, we synthesized the different shaped nanocrystals with the same coating molecule of SDS using the seed-mediated approaches.[33] Cube, cuboctahedron, octahedron and rhombic dodecahedron shapes formed due to the increasinge of the volumes of $NH_2OH_3{\cdot}HCl$ that change the amount of reductant added.[33] Cu_2O nanocrystals with cubic and rhombic dodecahedral structures were synthesized by adding presicely 9.55 mL, 9.35 mL, 9.05 mL, and 8.75 mL of deionized water respectively to four sample vials labeled a, b, c, and d, which were placed in a water bath at 32–34 °C. Then, 0.1 mL of a 0.1-M $CuCl_2$ solution and 0.087 g of SDS powder were added to each vial with vigorous stirring. After complete dissolution of the SDS powder, 0.20 mL of a 1.0-M NaOH solution was added, which turned the solution color into light blue immediately, due to the formation of $Cu(OH)_2$ precipitate. Finally, 0.15, 0.35, 0.65, and 0.95 mL of 0.2 M $NH_2OH_3{\cdot}HCl$ were quickly spiked within 5 s into vials a, b, c, and d, respectively. The total solution volume in each vial was now 10 mL. After the vials were stirred for 20 s, they were kept in the water bath at 37 °C for 2 h for nanocrystal growth. The suspension was centrifuged at 4000 ×*g* for 5 min. After the supernatant was decanted, the precipitate was washed with 6 mL of a 1:1 vol ratio of water and ethanol. The precipitate was centrifuged and washed again using the same water/ethanol mixture to remove unreacted chemicals and SDS. The final washing step used 5 mL of ethanol, and the precipitate was dispersed in 0.6 mL of ethanol for storage and analysis.

Morphology and Facet Indexing for different shaped Cu_2O

Scanning electron microscopy (SEM) images for four kinds of nanocrystal samples were taken by a field emission scanning electron microscope (FE-SEM) (JSM-7900 F, JEOL). Further facet identification and individual facet surface areas were determined statistically by a Verios 460 e Extreme High-Resolution Scanning Electron Microscope (XHR-SEM). At least 50 single nanocrystal particles of one kind were selected for XHR-SEM imaging. Titan Cubed Themis 300 double Cs-corrected Scanning/Transmission Electron Microscope (S/TEM) were operated to obtain the selected-area electron diffraction (SAED) patterns for facet identification. An X-ray diffraction (XRD, Philips, EMPYREAN, PANalytical Almelo, The Netherlands) equipped with a Co Kα radiation source measured the crystalline structure of the Cu_2O nanocrystals.

Facet-level analysis of surface properties

Work function determination by kelvin probe force microscopy (KPFM)

Work function is a direct consequence of the electrostatic barrier induced by the dipole double layer at the surface.[37] KPFM was used to obtain surface potential mapping on the Cu_2O nanocrystals to reveal the facet dependent surface electronic properties. The measured surface potential is the contact potential difference (CPD) due to the difference in work functions (or Fermi energy levels) between the sample surface and the tip. Surface work function is affected by surface charges, doping levels, defects or grain boundaries. KPFM was operated on a Bruker Dimension Icon® with the Frequency modulation KPFM integrated with PeakForce Tapping mode. Briefly, Platinum-Iridium (Pt/Ir) doped silicon cantilever probes (Bruker, USA) were used as the conductive probes that have a relative stable work function (Φ_{tip}),[38] a force constant of approximately 3 $N \cdot m^{-1}$ and a nominal resonance frequency of 75 kHz. Cu_2O nanocrystals were immobilized on Silicon wafers (∅3″ Silicon wafer, Type P/ < 111 >, TED PELLA, Inc.) by depositing 5 µL of the Cu_2O suspensions (10 $mg \cdot L^{-1}$) with ~30 min vacuum drying. During the operation, the microscope was fully contained in an environmental chamber with temperature (25 ± 2 °C) and humidity (< 10%). The sample surface's work function (Φ_{sample}) was calculated by CPD= $-(\Phi_{\text{tip}}$- $\Phi_{\text{sample}})/e$. To determine the work function of the tip (Φ_{tip}), we utilized three reference substrates, Au {111} substrate, highly oriented pyrolytic graphite (HOPG) and Si {111} substrates, which have stable work functions of 5.20–5.60 eV, 4.4–4.8 eV and 4.60–4.85 eV respectively. Each cantilever tip we used went through the same calibration process to determine the individual work function. At least 50 different facet regions of each shape on the deposited sample were probed to achieve statistical significance of the CPD measurement. More details about KPFM's tip calibration are provided in the section S1 in the supporting information.

Surface electrochemical activity measurement by AFM/SCEM

Besides KPFM, Cu_2O nanocrystals were also scanned for local surface electrochemical properties by the same Bruker AFM that was connected with a standard PeakForce SECM as introduced previously.[39] Prior to the PeakForce SECM measurement, all PeakForce SECM probes (Bruker Nano Inc, CA, US) were tested by performing cyclic voltammetry in a standard three-electrode electrochemical cell with a Pt counter electrode and a standard Ag/AgCl reference electrode. The electrochemical cell was filled with 1.8 mL of 10 mM $[Ru(NH_3)_6]Cl_3$ (one of commonly used redox couples for aqueous electrolytes to simulate fictive species reactions) in 0.1 M KCl. A bipotentiostat (CHI700E, CH Instrument) was connected to the electrochemical cell to perform the cyclic voltammetry analyses with a scanning voltage from 0 to − 0.4 V vs. Ag/AgCl at 50 $mV \cdot s^{-1}$ applied to the SECM probes. Both the probe and the sample on the substrate were working electrodes sharing the same reference and counter electrodes. The probe and the sample were biased at different potentials, relative to the reference electrode, to enable different chemical reactions. In this work, the probe reduces the $[Ru(NH_3)_6]^{3+}$ to $[Ru(NH_3)_6]^{2+}$ at − 400 mV versus a pseudo Ag/AgCl reference electrode, while the sample is biased at + 100 mV to oxidize $[Ru(NH_3)_6]^{2+}$ back to $[Ru(NH_3)_6]^{3+}$. We hypothesize that different dominant facets of Cu_2O should generate different levels of tip-sample currents at a sensitivity of $nA \cdot V^{-1}$ due to the reactivity differences and thus generate imaging contrast from the background or the silicon substrate that had negligible electrochemical oxidation reactions with $[Ru(NH_3)_6]^{3+}$. The PeakForce SECM scan was performed using an interleaved scan mode with a lift height of typically 40–150 nm between the probe and the sample surface. On each line scan during the main scan, the probe scans over the sample surface using the normal PeakForce QNM mode at a scan rate at 0.1 Hz and a scan size at 2 × 2 µm. After verifying SECM standard test sample (silicon nitride pattern cover on Pt layer) the sample-coated substrate was placed into the same fluidic cell to replace the SECM standard test sample. The same SCEM scanning procedure was performed on the sample surface at a DC bias of − 400 mV and + 100 mV applied to the probe and the sample substrate at the scan rate of 0.1 Hz and a scan size is 2 × 2 µm.

DFT calculations of surface properties

The Vienna Ab Initio Simulation Package (VASP) was used to perform all the density functional theory (DFT) calculations within the generalized gradient approximation (GGA) using the Perdew-Burke-Ernzerhof (PBE) formulation.[40,41] We employed projected augmented wave (PAW) potentials to describe the ionic cores and took valence electrons into account using a plane wave basis set with a kinetic energy cutoff of 500 eV.[42,43] Partial occupancies of the Kohn−Sham orbitals were allowed using the Gaussian smearing method with a width of 0.05 eV. The electronic energy was considered self-consistent when the energy change was smaller than 10^{-6} eV. A geometry optimization was considered convergent when the force change was smaller than 0.02 $eV \cdot Å^{-1}$. Grimme's DFT-D3 methodology was used to describe the dispersion interactions.[44].

The equilibrium lattice constants and atomic positions of a Cu_2O unit cell in the cubic $Pm\bar{3}m$ space group were optimized using a 6 × 6 × 6 Monkhorst-Pack k-point grid for Brillouin zone sampling. The {100}, {110} and {111} surfaces of Cu_2O were constructed with p (2 ×2 ×2) periodicity in the x, y and the z direction separated by a vacuum layer in the depth of 15 Å in order to separate the surface slab from its periodic duplicates. During structural optimizations, the $\mathbf{\Gamma}$ point in the Brillouin zone was used for k-point sampling.

The surface energy (γ_r) of Cu_2O facets can be described as:[37].

$$\gamma_r = \frac{(G_{surf} - \sum_i N_i \mu_i)}{A}, \tag{1}$$

where G_{surf} is the Gibbs free energy of the surface (eV), μ_i is the chemical potential of each species (eV) (in this case i = Cu and O), A is the surface area (m^2), and N_i represents the number of each species that the surface contains [45].

The work function was calculated by Eq. (2) to compare with the experimental data from KPFM using the equation.

$$\Phi = E_{vac} - E_f \tag{2}$$

where Φ is the work function (eV), E_{vac} is the electrostatic potential of vacuum level (eV), and E_f is the energy of Fermi level (eV).

The density of states (DOS) of the three Cu_2O nanocrystal facets were also calculated with an increased Monkhorst-Pack k-point mesh of 3 × 3 × 1. The adsorption energy (E_{ads}) of the adsorbate (i.e., H_2O or $\{Ru(NH_3)_6\}^{3+}$) is calculated by:

$$E_{ads} = E_{A/surf} - E_{surf} - E_{A(g)} \tag{3}$$

where $E_{A/surf}$, E_{surf} and $E_{A(g)}$ are the energy of the adsorbate molecules on the surface (eV), the energy of clean surface (eV), and the energy of isolated A molecule (eV) in a cubic periodic box with a side length of 20 Å and a 1 × 1 × 1 Monkhorst-Pack k-point grid for Brillouin zone sampling, respectively. The atomic charges were obtained from Bader charge calculations and analysis based on the numerical implementation developed by Henkelman et al.[46].

Results and discussions

Morphology and crystallographic facet indexing

The top panel of Fig. 1 shows high resolution SEM images of four different Cu_2O nanocrystals, which have comparable morphologies with previously reported results.[47] For example, cubic nanocrystals are generally composed of six identical square {100} facets. Cuboctahedron nanocrystals have six squares {100} facets in addition to the eight {111} facets. Octahedral nanocrystals are those with an octahedral structure bound by only {111} facets. There are twelve congruent rhombic {110} facets in a rhombic dodecahedron.

The insert of top row illustrates the 3-D models of the four shaped nanocrystals. The second row shows their typical TEM images. The third row shows SAED images. For a cubic particle made of six exposed {100} facets, when the electron beam was aligned to be perpendicular to the direction of the [001], a two-dimensional (2-D) square-shaped projection should be observed in the TEM image. Four facets in the {100} family, which are parallel to [001] zone axis,

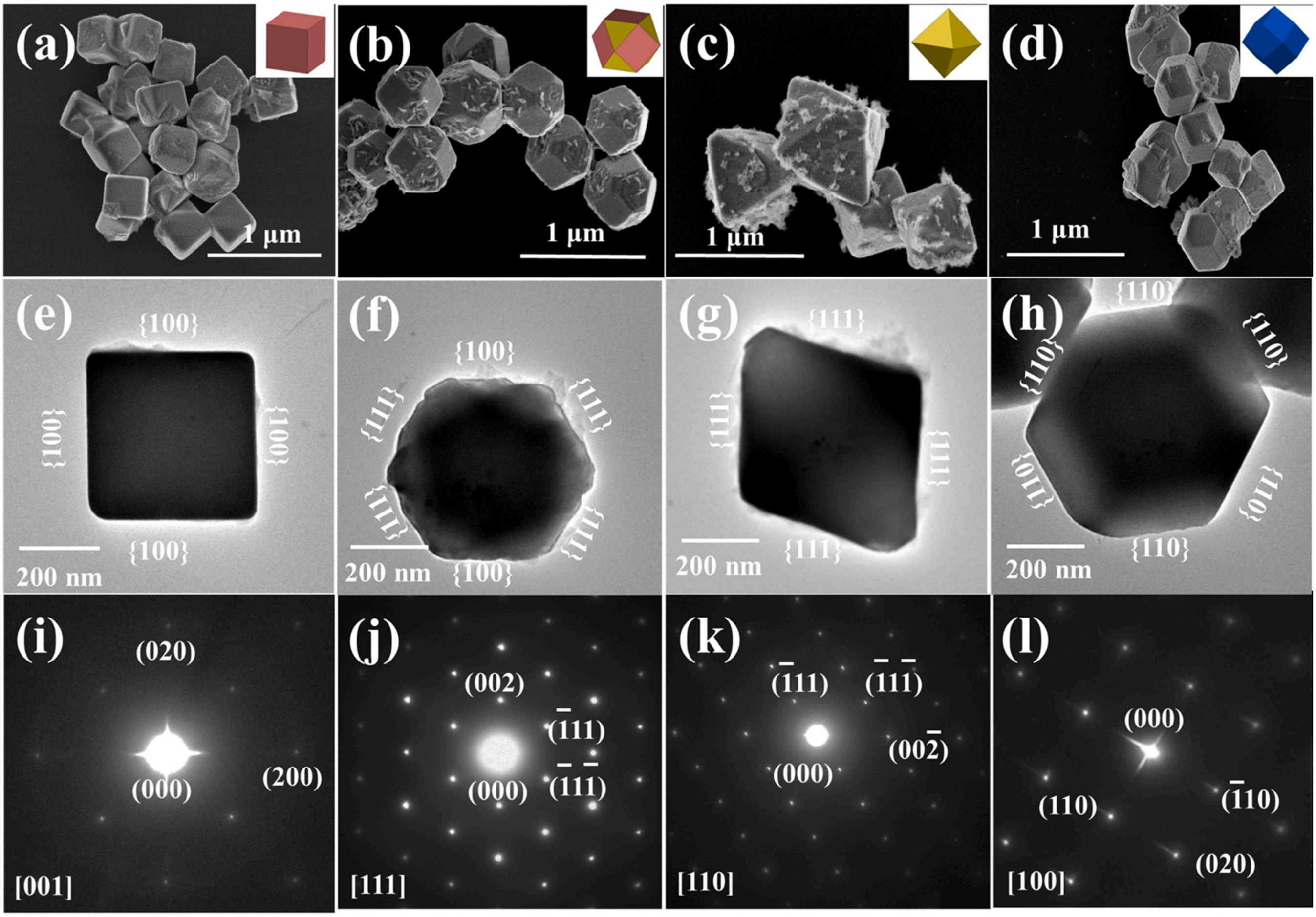

Fig. 1. SEM images, sketch, bright TEM images and corresponding SAED patterns of the Cu_2O nanocrystals with various morphologies: cube, cuboctahedron, octahedron, and rhombic dodecahedron.

are marked in Fig. 1**e**. The HR-TEM images and the index of the spots in the SAED patterns indicate that this Cu_2O nanocrystal product is a single crystal and these cubes mainly have their (100) crystal facets exposed, which can also be evidenced by the XRD patterns (Fig. S8).

As for a cuboctahedron bounded by six square {100} and eight triangle {111} facets, when the electron beam is aligned to be perpendicular to [111], the TEM image exhibits as an equilateral hexagon projection constructed by the edges of {100} and {110}. The corresponding diffraction patterns in Fig. 1**j** and XRD pattern in Fig. S8 demonstrate the existence of {100} and {111} facets. The SAED pattern of Cu_2O cuboctahedron gives two sets of lattice fringes of 0.21 nm and 0.246 nm with an intersection angle of 60°. These lattice fringes correspond to the lattice fringe of the $(\bar{1}11)$ and (002) planes of the Cu_2O structure respectively (JCPDS card No. 34–1354).[48].

For an octahedral particle in Fig. 1**g**, the projection is a parallelogram made of the projections of four {111} facets if the electron beam is in parallel with the [110] zone axis. The SAED pattern of Cu_2O octahedron gives two sets of lattice fringes of 0.246 nm with an intersection angle of 60°. These lattice fringes respectively correspond to the lattice fringe of the $(\bar{1}11)$ and $(\bar{1}1\bar{1})$ planes of the Cu_2O structure (JCPDS card No. 34–1354), and XRD pattern (Fig. S8) further indicates that octahedral Cu_2O is composed of single crystals and these crystalline octahedrons mainly have their {111} crystal facets exposed.

For a rhombic dodecahedron particle in Fig. 1**h**, the TEM projection is a hexagon shape if viewed from [110] zone axis. The six edges of the hexagon correspond to the edge of {110}. The lattice fringe of 0.30 nm of rhombic dodecahedron can be assigned to the (110) plane of the Cu_2O structure. The SEAD pattern and XRD measurements reveal that rhombic dodecahedron mainly exposes the {110} facets of the single crystal.

Facet-Dependent Work Function

Work functions was measured by KPFM on single Cu_2O nanocrystals to reveal the different electronic structures of the {100}, {110}, and {111} facets. Fig. 2**a** shows the surface potential mapping of different Cu_2O nanocrystals deposited on the silicon wafer. Based on the analysis of over 15 different single nanocrystals for each shape, the surface potentials (or the CPD levels) are estimated to + 320 ± 50, + 350 ± 70, and + 400 ± 58 mV for the {100}, {110}, and {111} facet-dominant surfaces, respectively. The corresponding surface work function of {100}-cubic, {110}-rhombic dodecahedral, and {111}-octahedral Cu_2O are calculated to be 4.92, 4.95, and 5.00 eV, respectively. As previous study reported that the {100} and {110} facet surfaces of Cu_2O both had the lowest work functions, which supports our observation.[49] For the cuboctahedron Cu_2O nanocrystals, we observed a difference between {100} and {111} surfaces of ~80 mV. This surface potential difference could, in turn, lead to the formation of an electronic surface junction or Schottky barrier that influences charge transfer across the solid interface. Compared with the {100} and {111} facets, the {110} facet possesses the intermediate electronic work function.

The DFT simulation results reveal that four Cu_2O nanocrystals elicit different surface structures and thus different work functions. For instance, the presence of highly electronegative atoms, such as

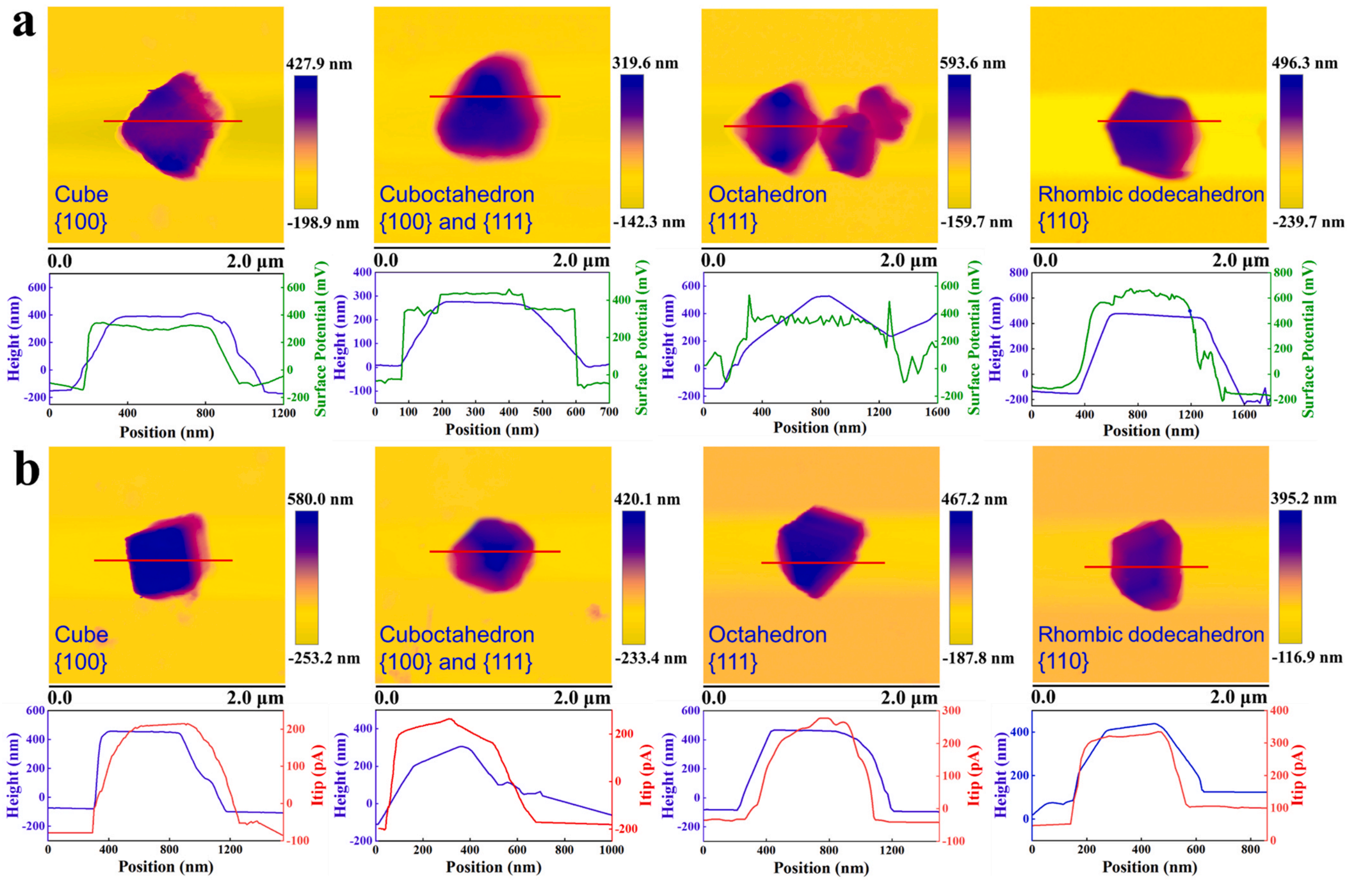

Fig. 2. (a) Morphology and cross-sectional surface potentials along the red lines in top images for four Cu_2O nanocrystals. (b) Typical topography and AFM-SECM cross-sectional tip-sample current along the red lines in top images for four Cu_2O nanocrystals.

Table 1
The calculated relaxed surface energies (γ_r), work functions (Φ), and the bandgaps (E_g) of different Cu_2O surfaces, the bandgaps (E^*_g) of the $[Ru(NH_3)_6]^{3+}$ adsorption on different Cu_2O surfaces, the adsorption energies (E_{ads}) of the H_2O and $[Ru(NH_3)_6]^{3+}$ adsorption on different Cu_2O surfaces and the charge transfer between $[Ru(NH_3)_6]^{3+}$ cation and different Cu_2O surfaces.

Surface	γ_r ($J{\cdot}m^{-2}$)	Φ (eV)	E_g (eV)	E^*_g (eV)	E_{ads} (H_2O) (eV)	E_{ads} ($[Ru(NH_3)_6]^{3+}$) (eV)	Charge transfer (e)
{100}:Cu	1.12	4.48	0.46	0.14	−1.28	−4.21	−0.76
{100}:O	1.05	5.58	0.97	0.56	−1.72	−4.86	−0.70
{110}:Cu	2.12	3.93	–	–	−2.95	−9.93	−1.11
{110}:Cu-O	2.09	5.66	–	–	−0.75	−4.44	−0.49
{111}:Cu	2.01	4.82	0.59	0.32	−1.77	−4.10	−0.58
{111}:O	1.87	4.67	0.49	0.45	−1.80	−4.59	−0.52

oxygen, at the surface increases the contribution of the dipole double layer to this electrostatic barrier, making it harder for an electron to leave the surface. As such, both the {100}:O and {110}:Cu-O structures were found to render significantly higher work functions than the only Cu-terminated surfaces. Conversely, the work function of the {110}:Cu structure is smallest in value when compared to that of other surfaces, which may result in the increased electron transfer. In addition, a comparison between the measured work function by KPFM in Fig. 2**a** and the DFT simuliations in Table 1 shows that the calculated work functions of the {100}:O, the {110}:Cu-O, and the {111}:Cu are very close to the KPFM results. The minor discrepancies could result from the surface adsorption of water molecules present in the ambient air that forms a dipole layer and affects an effective surface potential.[50] The average DFT-computed work functions for each surface termination are, in general, in agreement with the experimental measurements; however, the surface electronic structure of the three Cu_2O nanocrytal are too complex to be precisely modeled and calculated. The work function measurement indicates that Cu_2O nanocrystals also exhibit facet-dependent work functions, which may affect the interfacial charge transfer and the molecular interactions.[51] For example, the measured work function of {110}-rhombic dodecahedral is lower than that of {111}-octahedral Cu_2O. This result matches the first-principles calculations in adsorption energies (E_{ads}) and charge transfer calculations.

Facet-dependent electrochemical activity

Local electronic structures could influence the solvent/electrolyte properties and double layer effects on surface electrochemical processes or reactions of Cu_2O nanocrystals. The topography and cross-sectional tip-sample current of four types of Cu_2O nanocrystals are compared in Fig. 2**b**. The tip current image contrast was generated due to the enhanced reduction reaction of $[Ru(NH_3)_6]^{3+}$ to $[Ru(NH_3)_6]^{2+}$ with a DC bias potential at −0.4 V applied to the tip, which has a tip radius of 25 nm and a tip height of 215 nm. As depicted in Fig. S2e, when the tip approached the sample surface, the tip current increased due to the enhanced oxidation reaction of $[Ru(NH_3)_6]^{2+}$ at the Cu_2O surface under a positive DC bias (+0.1 V). The oxidized product then diffused to the tip for reductive reactions, which led to a higher tip current. In Section S2, we analzyed the effect of tip-sample distance on the measured tip current, which shows the concentration of $[Ru(NH_3)_6]^{3+}$ at the tip surface decreased with the tip-sample distance. By contrast, the silicon substrate, though under the same positive DC bias, did not exhibit the same oxidative reactivity toward $\{Ru(NH_3)_6\}^{2+}$ and thus generated a relatively low tip current enhancement.

Furthermore, Fig. 2**b** shows that the tip-sample current exhibited slight dependence on the shape or exposed facets of Cu_2O nanocrystals. Cube, cuboctahedron, octahedron and rhombic dodecahedron of Cu_2O nanocrystals yielded an average tip current of 205.4 ± 16.4, 233.4 ± 26.8, 279.4 ± 25,2 and 318.3 ± 17.8 pA, respectively, at the same tip-sample distance of 100 nm. The observed shape dependence of tip currents supports our speculation of the effects of different facet surface states (e.g., work functions) on electrolyte/electrode interactions. For instance, the diffusion and concentration profile or distribution of the redox mediator from the bulk solution to the probe tip could be affected by the local interactions of mediator molecules and facet surfaces.[52] The interplay or overlapping of the two electric double layers of the samples and the probes affects the diffusion transport of the redox mediators and ultimately the redox reactions at the tip (or tip current). Fig. S2d shows that the tip captured a slightly higher effective surface concentration (C_d) of the redox mediator when approaching the {110} facet of Cu_2O compared with {100} and {111} facets. This higher tip current resulted from the faster loop reaction rates of the redox mediators between the tip and the sample surface as illustrated Fig. S2e.

Traditional electrochemical activity assessment of Cu_2O nanocrystals

Cyclic Voltammetry (CV) could potentially reveal the “fingerprint” of specific lattice planes of nanoparticles such as gold,[53] CeO_2[54] and Co_3O_4.[55] For instance, the oxidation peak for {100} and {111} of gold nanostructures in 0.01 M aqueous H_2SO_4 were reported to be + 1.3 and + 1.1 V (vs Ag/AgCl, saturated KCl), respectively.[56] To compare with the results from AFM/SECM, CV curves were obtained for the four types of Cu_2O nanocrystals as detailed in Section S3. Fig. 3**a** shows the typical CV curves that exhibit different peak currents at corresponding applied potentials. For Cu_2O nanocubes, a clear oxidation peak and a reduction peak is noted at around + 0.38 V and + 0.29 V (vs Ag/AgCl, 1.0 M KCl), respectively. Cu_2O nanocubes have a peak-to-peak potential separation or the difference between the oxidation and reduction peak potentials (ΔE_p,) of 113 mV (vs. Ag/AgCl) with relatively low redox peak currents, due to the presence of the dominant {100} facets as shown in the HR-TEM results (Fig. 1**i**). For cubooctahedron, the CV peaks are determined by the {111} and {100} facets. The oxidation peak current of Cu_2O cuboctahedron is slightly higher that of Cu_2O nanocubes, probably because the {111} plane of Cu_2O promoted the electron transfer or reactivity toward the probe molecules of $[Fe(CN)_6]^{3-/4-}$. On the octahedron, a pair of well-defined redox peaks also appear with the ΔE_p of 103 mV, due to the increase of the {111} plane. Similarly, rhombic dodecahedron achieved a lower ΔE_p of 87 mV (vs. Ag/AgCl), indicating a higher charge-transfer ability and a more reversible electron transfer process on the electrode surface. The larger ΔE_p values, the higher energy barrier present for the electron transfer and thus electrochemical reactions become more irreversible. Fig. S3 compares that for all the scan rate (ν) studied, the ratio of the cathodic and anodic processes' peak currents is consistently nearing 0.95, indicating the chemical reversibility as expected for the $[Fe(CN)_6]^{3-/4-}$ redox process. Furthermore, the Fig. 3**b** shows that from 10 to 500 $mV{\cdot}s^{-1}$, the peak currents density had a linear relationship with square root of scan rate ($\nu^{1/2}$), demonstrating the classical Nernstian diffusion-controlled redox behavior.

Fig. 3**d–g** further compares the EIS complex-plane plots for the four types of Cu_2O nanocrystal-covered Au/Cu electrodes at an open-circuit potential in 5 mM $K_3[Fe(CN)_6]$ with 0.1 M KCl solution in the frequency range from 0.1 to 10^6 Hz. The semicircle portion at high frequencies characterizes the electron transfer limited process and the linear portion at lower frequencies results from a diffusion limited process. The distorted semicircle suggests that a double layer was established at the interface of electrolyte/Cu_2O nanocrystals on Au/Cu electrode. Smaller semicircle usually means faster interfacial charge transfer.[57] Moreover, Cu_2O nanocrystals-coated electrodes possessed smaller semicircle than that after methyl orange (MO) adsorption, which could increase the interfacial electric resistance. Details about MO adsorption on Cu_2O are provided in section S4.

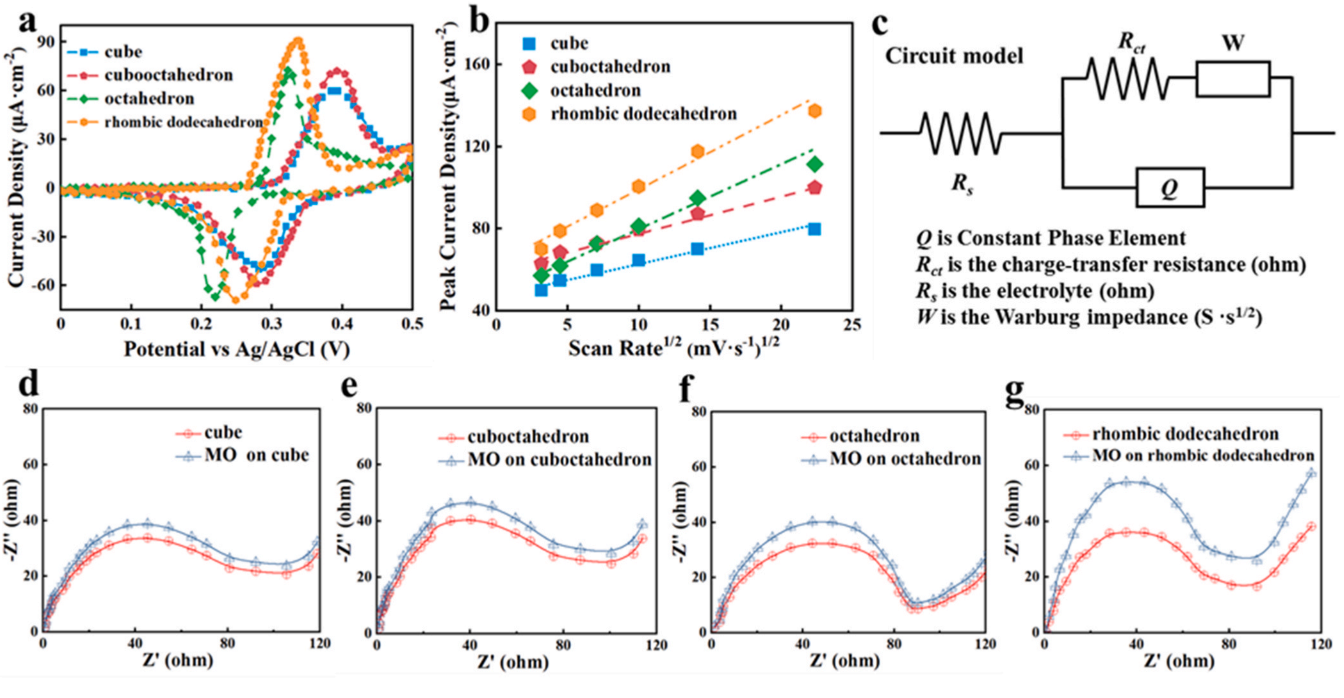

Fig. 3. (a) Characteristic cyclic voltametric curves of fourCu_2O nanocrystals under 50 $mV{\cdot}s^{-1}$ scan rate (ν) in 5 mM $K_3\{Fe(CN)_6\}$ with 0.1 M KCl solution. (b) The peak current plots versus the square root of scan rates ($\nu^{1/2}$) (from 10 to 500 mV/s). (c) Equivalent circuit used to fit the Nyquist plots obtained via EIS. Nyquist impedance plots for the pristine Cu_2O nanocrystal-coated electrodes and those after methyl orange (MO)-adsorption: (d) cube, (e) cuboctahedra, (f) octahedra and (g) rhombic dodecahedra.

To quantify the interfacial resistance changes, the charge transfer resistance (R_{ct}) was obtained by fitting the impedance data to an equivalent electric circuit model (Fig. 3**c**). Table S2 shows that R_{ct} increased from 104.1 ± 0.50 Ω to 112.2 ± 0.36 Ω before and after MO adsorption for the cubic Cu_2O nanocrystals. By contrast, upon deposition of cuboctahedron Cu_2O nanocrystals on the Au/Cu electrode, the R_{ct} value decreased to 89.7 ± 0.10 Ω, indicating that the increased {111} facet facilitated electron transfer of the interfacial redox reactions. R_{ct} for the rhombic dodecahedron nanocrystal modified Au/Cu electrode further decreased to 70.19 ± 0.18 Ω and achieved the faster electron transfer rate than cube, cuboctahedron and octahedron Cu_2O. This result matches the observed facet-dependent photocatalytic properties of Cu_2O nanocrystals, where rhombic dodecahedron with dominant {110} facets was reported to achieve greater efficiency of radical production, than octahedron and cube with dominant {111} and {100} facets respectively.[58,59] The range of n (0.85–0.96) for CPE further confirms that these electrode interface should be treated as an imperfect capacitor with non-ideal behavior of capacitance due to surface heterogeneity. Moreover, Table S2 shows that the relative change of R_{ct} before and after MO adsorption is different, suggesting different adsorption ability of MO for four different Cu_2O nanocraystals as supported by Fig. S4b.

Mechanism analysis for facet-dependence of surface electronic and electrochemical properties

Surface energy and adsorption energy

We have calculated the surface energies of the six different surface terminations as shown in Table 1. First, the three low-index Cu_2O surfaces: {100}, {110} and {111}, were constructed with each terminated in two ways as illustrated in Fig. 4**a**. The surface energy of {100}:Cu and the {100}:O are similar (1.12 and 1.05 $J\cdot m^{-2}$, respectively). Only O atoms are terminated in the {100}:O facet, which has a slightly lower surface energy than the Cu terminated facet. The {110}:Cu and {110}:Cu–O have the highest surface energies of 2.12 and 2.09 $J\cdot m^{-2}$ respectively. Finally, we found a surface energy of 1.87 $J\cdot m^{-2}$ for the {111}:O surface that is slightly lower than that of {111}:Cu (2.01 $J\cdot m^{-2}$). Clearly, surface energy increases with the increase of under-coordinated Cu atoms as reported previously.[60] This {111}:O surface contains both doubly coordinated Cu atoms and undercoordinated, singly coordinated Cu atoms, with dangling bonds perpendicular to the surface. The {111}:Cu surface similarly exposes both Cu atoms and O atoms, but the density of dangling bonds is much less than the {110} surface. The surface energies of Cu_2O generally follow the density of undercoordinated Cu atoms, {100} < {111} < {110}.[61] A higher surface energy typically indicates a more reactive surface[62] and therefore the highest surface energy of each facet correlates with the observed adsorptive performance of the Cu_2O nanocrystals, as measured on the cubic {100} crystals, octahedral {111} crystals, and rhombic dodecahedral {110} crystals.

Adsorption energies of $[Ru(NH_3)_6]^{3+}$ on the Cu_2O {100}, {110} and {111} surfaces are compared to explain and support the facet-dependent electrochemical reactivity. Fig. S5 shows the most stable adsorption configurations with different surface atomic bonding. The adsorption energies (E_{ads}) of $[Ru(NH_3)_6]^{3+}$ on all of the three crystal facets were negative, suggesting the adsorption processes could be exothermic and spontaneous. The adsorption energy, E_{ads}, correlates strongly with the surface energy (γ_r), as shown in Table 1. For both adsorbates (H_2O and $[Ru(NH_3)_6]^{3+}$), the {110} surface shows the strongest average adsorption energy, in agreement with the measured electrochemical activity.

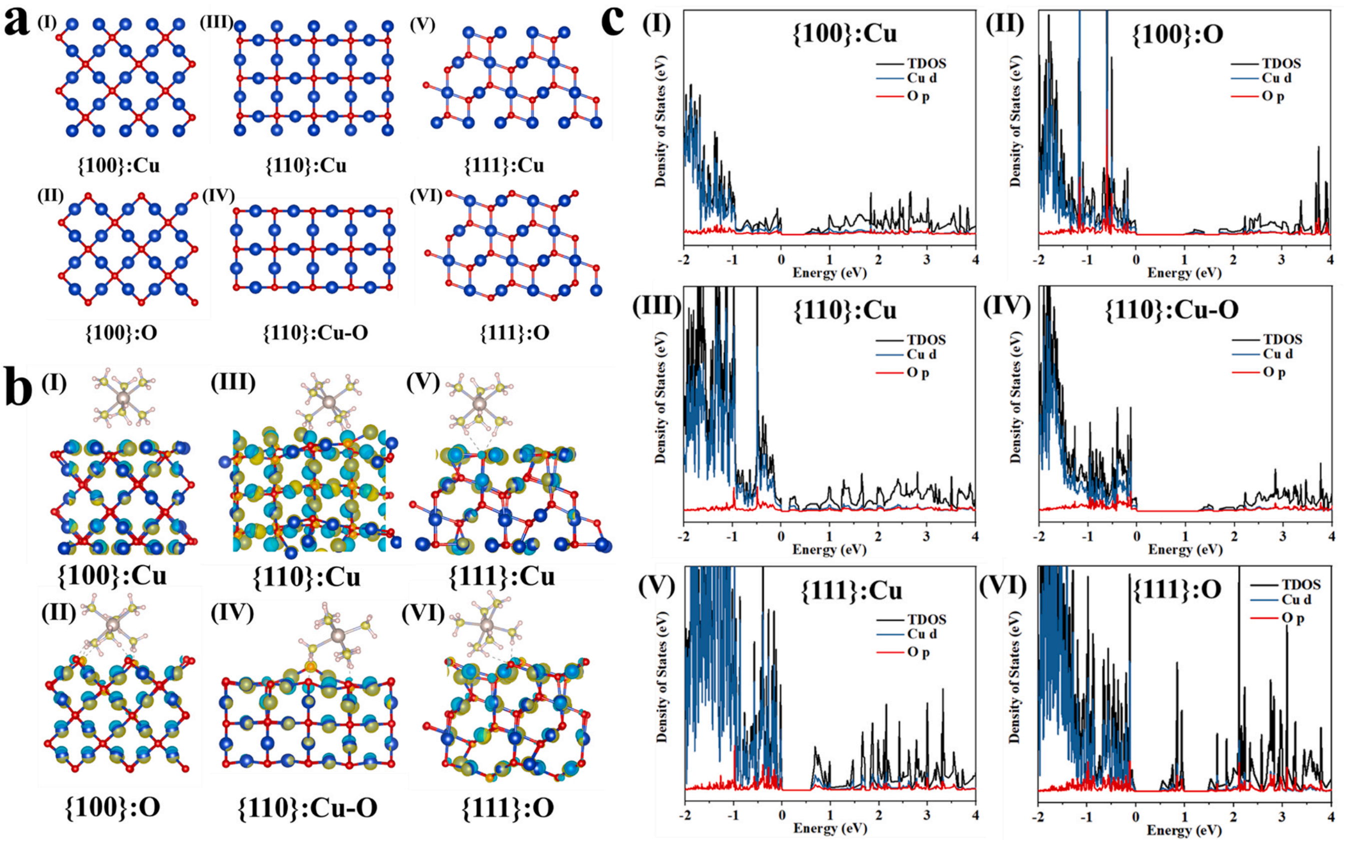

Fig. 4. (a) Relaxed Cu_2O surfaces. (b) Three dimensional charge density difference maps of $[Ru(NH_3)_6]^{3+}$ cation on Cu_2O surfaces (yellow: electron accumulation; cyan: electron depletion) Blue, red, gray, light blue, pink balls indicate Cu, O, Ru, N and H atoms, respectively. (c) Electronic DOS of Cu_2O surfaces.

Bader charge analysis

To further investigate the electronic interactions between $[Ru(NH_3)_6]^{3+}$ and different crystal facets of Cu_2O, the charge transfer was also assessed for the adsorption of $[Ru(NH_3)_6]^{3+}$ and summarized listed in Table 1**.** Fig. 4**b** shows that there is obvious electron injection from different Cu_2O surfaces to $[Ru(NH_3)_6]^{3+}$ cation as indicated that all N atoms are surrounded by yellow lobes that represent charge accumulation. The more charge transfer between $[Ru(NH_3)_6]^{3+}$ and these surfaces, the stronger the electronic interactions that form, which will lead to better catalytic activity. Thus, the {110}:Cu facets yielded a greater strength of electronic interaction with $[Ru(NH_3)_6]^{3+}$ than other facets, {100} facets and {111} facets as indicated by the lower charge transfer. The results explain the distinct reaction rates of $[Ru(NH_3)_6]^{3+}$ on different Cu_2O facets.

Density of states analysis

The calculated projected density of states (DOS) shows that both valence band maxima (VBM) and conduction band minima (CBM) mainly consist of O (p) and Cu (d) orbitals, respectively, while contributions from other orbitals are much less. The electronic band gaps (E_g) of the three low-index Cu_2O surfaces with different surfaces terminations are determined from the (DOS) as the difference between the valence band maximum (VBM) and conduction band minimum (CBM), and are summarized in Table 1.

Fig. 4**c** shows that for {100}:Cu there is a small band gap of 0.46 eV, while the {100}:O surface shows a much larger band gap of 0.97 eV. We observed a finite number of states near the Fermi level in the electronic DOS of the {110}:Cu and {110}:CuO surfaces and hence propose that these surfaces are conducting. We also found that the bandgaps for the {111} surfaces are quite low; the {111}:Cu and {111}:O terminated surfaces are found to have band gaps of 0.59 eV and 0.49 eV, respectively. These results are in agreement with Soon et al., who employed the technique of “ab initio atomistic thermodynamics” to identify the surface structures of the {110} and {111} planes under oxygen-rich and oxygen-lean conditions.[37] Comparing the appropriate surfaces from that work with ours, we find agreement for the {110} and {111} cases; furthermore, their study indicated that these states are true metallic surface states. These metallic states at the Fermi level should make electron transfer more facile on the {110} surface compared to the {111} or {100}, further explaining the observed enhanced activity.

Finally, comparison of the bandgaps before and after adsorption of $[Ru(NH_3)_6]^{3+}$ on Cu_2O surfaces suggests that the adsorption of $[Ru(NH_3)_6]^{3+}$ could narrow the bandgap mainly due to the presence of the N (p) impurity state as shown in the DOS of each Cu_2O surface after $\{Ru(NH_3)_6]^{3+}$ adsorption (Fig. S7). This N (p) impurity alter the band structure and the corresponding DOS of all Cu_2O surfaces and also facilitate charge transfer for each surfaces.

Conclusion

With different facets exposing different surface atoms, tuning Cu_2O morphology correspondingly controls its surface chemistry and reactivity. Depending on the atomic coordination and structural configuration of Cu_2O surfaces, different proportions of cations and anions are accessible for molecular adsorption or reactions. Furthermore, different atomic coordination results in instrinc properties such as distinct electron density configurations and band gap energies or structures, which also influence the type and strength of molecular interactions on facets. Because these electronic and molecular interaction characteristics govern the mechanisms in heterogeneous catalysis, gas sensing, or electrochemical reactions, the facet control or engineering holds paramount importance in functional nanomaterial systhsis and applications.

In this work, for the first time, KPFM and AFM-SECM demonstrated the nanoscale facet dependent electronic and electrochemical properties of Cu_2O nanocrystals with different exposed facets. We employed traditional electrochemical measurement including cyclic voltammetry and electrochemical impedance spectroscopy to confirm facet dependent electrochemical properties of Cu_2O nanocrystals. Lastly, DFT calculations revealed that the higher surface energy and efficient electron transfer on {110} facet responsible for the higher electrochemical responses. The AFM-SECM technique should be applicable in the study of other electrochemical systems. Because it is based on a scanning-probe platform, the technique is suited for understanding heterogeneity in surface or interface electrochemical response (although not fully exploited in this work, our preliminary results indicate that this is possible). The technique could also provide insight into understanding the operation of batteries, fuel cells and other electrochemical systems.

CRediT authorship contribution statement

Qingquan Ma: Methodology, investigation and writing original draft preparation, **Joshua Young**: Supervision, writing, reviewing and editing, **Sagnik Basuray**: Reviewing and editing, **Guangming Cheng**: TEM analysis and writing, **Jianan Gao:** TOC design and data analysis, **Nan Yao:** Reviewing and editing, **Wen Zhang**: Supervision, Conceptualization, writing, reviewing and editing.

Data Availability

Data will be made available on request.

Declaration of Competing Interest

The authors declare that they have no known competing financial interests or personal relationships that could have appeared to influence the work reported in this paper.

Acknowledgements

This study is supported by the US National Science Foundation (Award#: 1756444), NSF INTERN grant (Award number: 1836036) and the New Jersey Water Resources Research Institute (NJWRRI) Grant (Project Number: 2020NJ025B). Moreover, the authors also thank Princeton’s Imaging and Analysis Center and the Princeton Center for Complex Materials, a National Science Foundation (NSF)-MRSEC program (DMR-1420541). DFT calculations were performed on the Kong and Lochness clusters at the New Jersey Institute of Technology, the Extreme Science and Engineering Discovery Environment (XSEDE, supported by NSF Grant No. ACI-1053575) under allocation TG-DMR180009, and the CARBON cluster at the Center for Nanoscale Materials under allocations CNM72868 and CNM77374. Work performed at the Center for Nanoscale Materials, a U.S. Department of Energy Office of Science User Facility, was supported by the U.S. DOE, Office of Basic Energy Sciences, under Contract No. DE-AC02–06CH11357.

Appendix A. Supporting information

Supplementary data associated with this article can be found in the online version at doi:10.1016/j.nantod.2022.101538.

References

[1] G. Liu, H.G. Yang, J. Pan, Y.Q. Yang, G.Q. Lu, H.-M. Cheng, Chem. Rev. 114 (2014) 9559–9612.

[2] H.E. Rudel, M.K.M. Lane, C.L. Muhich, J.B. Zimmerman, ACS nano 14 (2020) 16472–16501.

[3] Y.A. Wu, I. McNulty, C. Liu, K.C. Lau, Q. Liu, A.P. Paulikas, C.-J. Sun, Z. Cai, J.R. Guest, Y. Ren, Nat. Energy 4 (2019) 957–968.

[4] A.W. Lounsbury, R. Wang, D.L. Plata, N. Billmyer, C. Muhich, K. Kanie, T. Sugimoto, D. Peak, J.B. Zimmerman, J. Colloid Interface Sci. 537 (2019) 465–474.
[5] B.-R. Chen, L.A. Crosby, C. George, R.M. Kennedy, N.M. Schweitzer, J. Wen, R.P. Van Duyne, P.C. Stair, K.R. Poeppelmeier, L.D. Marks, Acs Catal. 8 (2018) 4751–4760.
[6] T. Wu, N. López, T. Vegge, H.A. Hansen, J. Catal. 388 (2020) 1–10.
[7] A.-T. Lee, C.-S. Tan, M.H. Huang, ACS Cent. Sci. 7 (2021) 1929–1937.
[8] C.-S. Tan, M.H. Huang, Inorg. Chem. Front. 8 (2021) 4200–4208.
[9] A.S. Patra, J.-C. Kao, S.-J. Chan, P.-J. Chou, J.-P. Chou, Y.-C. Lo, M.H. Huang, J. Mater. Chem. C. 10 (2022) 3980–3989.
[10] S. Weon, M.-J. Suh, C. Chu, D. Huang, E. Stavitski, J.-H. Kim, ACS EST Eng. 1 (2021) 512–522.
[11] W. Zhu, R. Michalsky, On Metin, H. Lv, S. Guo, C.J. Wright, X. Sun, A.A. Peterson, S. Sun, J. Am. Chem. Soc. 135 (2013) 16833–16836.
[12] Y.-K. Peng, Y. Hu, H.-L. Chou, Y. Fu, I.F. Teixeira, L. Zhang, H. He, S.C.E. Tsang, Nat. Commun. 8 (2017) 1–13.
[13] X. Huang, Y. Chen, E. Walter, M. Zong, Y. Wang, X. Zhang, O. Qafoku, Z. Wang, K.M. Rosso, Environ. Sci. Technol. 53 (2019) 10197–10207.
[14] Y.-K. Peng, S.E. Tsang, Nano Today 18 (2018) 15–34.
[15] S. Chen, T. Cao, Y. Gao, D. Li, F. Xiong, W. Huang, J. Phys. Chem. C. 120 (2016) 21472–21485.
[16] J. Sung, B.K. Choi, B. Kim, B.H. Kim, J. Kim, D. Lee, S. Kim, K. Kang, T. Hyeon, J. Park, J. Am. Chem. Soc. 141 (2019) 18395–18399.
[17] Y. Jiang, T. Xia, L. Shen, J. Ma, H. Ma, T. Sun, F. Lv, N. Zhu, A.C.S. Catalysis, 11 (2021) 2949–2955.
[18] R. Gao, J. Zhu, X. Xiao, Z. Hu, J. Liu, X. Liu, J. Phys. Chem. C. 119 (2015) 4516–4523.
[19] K. Chennit, J. Trasobares, As Anne, E. Cambril, A. Chovin, N. Clément, C. Demaille, Anal. Chem. 89 (2017) 11061–11069.
[20] K. Huang, A. Anne, M.A. Bahri, C. Demaille, ACS nano 7 (2013) 4151–4163.
[21] J. Jiang, Z. Huang, C. Xiang, R. Poddar, H.J. Lewerenz, K.M. Papadantonakis, N.S. Lewis, B.S. Brunschwig, ChemSusChem 10 (2017) 4657–4663.
[22] P. Knittel, B. Mizaikoff, C. Kranz, Anal. Chem. 88 (2016) 6174–6178.
[23] S. Kolagatla, P. Subramanian, A. Schechter, Appl. Catal. B: Environ. 256 (2019) 117843.
[24] S. Kolagatla, P. Subramanian, A. Schechter, ChemSusChem 12 (2019) 2708–2714.
[25] L.-L. Ma, J.-L. Li, H.-Z. Sun, M.-Q. Qiu, J.-B. Wang, J.-Y. Chen, Y. Yu, Mater. Res. Bull. 45 (2010) 961–968.
[26] G. Liu, F. Zheng, J. Li, G. Zeng, Y. Ye, D.M. Larson, J. Yano, E.J. Crumlin, J.W. Ager, L.-w Wang, Nat. Energy 6 (2021) 1124–1132.
[27] J. Kadowaki, T. Jones, A. Sengupta, V. Gopalan, V. Subramaniam, Sci. Rep. 11 (2021) 1–12.
[28] L. Gao, Z. Qiu, W. Gan, X. Zhan, J. Li, T. Qiang, Sci. Rep. 6 (2016) 1–10.
[29] H. Zhang, Q. Zhu, Y. Zhang, Y. Wang, L. Zhao, B. Yu, Adv. Funct. Mater. 17 (2007) 2766–2771.
[30] J. Zhang, J. Liu, Q. Peng, X. Wang, Y. Li, Chem. Mater. 18 (2006) 867–871.
[31] L. Chen, Y. Zhang, P. Zhu, F. Zhou, W. Zeng, D.D. Lu, R. Sun, C. Wong, Sci. Rep. 5 (2015) 9672.
[32] J. Xiang, Z. Chen, J. Wang, Mater. Res. Bull. 70 (2015) 456–460.
[33] Z.G. Liu, Y.F. Sun, W.K. Chen, Y. Kong, Z. Jin, X. Chen, X. Zheng, J.H. Liu, X.J. Huang, S.H. Yu, Small 11 (2015) 2493–2498.
[34] T. Wu, H. Zheng, Y. Kou, X. Su, N.R. Kadasala, M. Gao, L. Chen, D. Han, Y. Liu, J. Yang, Microsyst. Nanoeng. 7 (2021) 1–10.
[35] J. Shi, J. Li, X. Huang, Y. Tan, Nano Res. 4 (2011) 448–459.
[36] L. Pan, Y. Liu, L. Yao, D. Ren, K. Sivula, M. Grätzel, A. Hagfeldt, Nat. Commun. 11 (2020) 1–10.
[37] A. Soon, M. Todorova, B. Delley, C. Stampfl, Phys. Rev. B 75 (2007) 125420.
[38] R.F. Gouveia, F. Galembeck, J. Am. Chem. Soc. 131 (2009) 11381–11386.
[39] X. Shi, Q. Ma, T. Marhaba, W. Zhang, JoVE (J. Vis. Exp.) (2021) e61111.
[40] G. Kresse, J. Furthmüller, Phys. Rev. B 54 (1996) 11169.
[41] J.P. Perdew, K. Burke, M. Ernzerhof, Phys. Rev. Lett. 77 (1996) 3865.
[42] G. Kresse, D. Joubert, Phys. Rev. b 59 (1999) 1758.
[43] P.E. Blöchl, Phys. Rev. B 50 (1994) 17953.
[44] T. Bucko, J. Hafner, S. Lebegue, J.G. Angyán, J. Phys. Chem. A 114 (2010) 11814–11824.
[45] L.-Y. Gan, R.-Y. Tian, X.-B. Yang, Y.-J. Zhao, J. Chem. Phys. 136 (2012) 044510.
[46] G. Henkelman, A. Arnaldsson, H. Jónsson, Comput. Mater. Sci. 36 (2006) 354–360.
[47] C.-H. Kuo, M.H. Huang, Nano Today 5 (2010) 106–116.
[48] X. Zhang, Y. Zhang, H. Huang, J. Cai, K. Ding, S. Lin, N. J. Chem. 42 (2018) 458–464.
[49] S. Lee, C.-W. Liang, L.W. Martin, ACS nano 5 (2011) 3736–3743.
[50] W. Zhang, J. Hughes, Y. Chen, Appl. Environ. Microbiol. 78 (2012) 3905–3915.
[51] J. Lin, W. Hao, Y. Shang, X. Wang, D. Qiu, G. Ma, C. Chen, S. Li, L. Guo, Small 14 (2018) 1703274.
[52] M. Choi, N.P. Siepser, S. Jeong, Y. Wang, G. Jagdale, X. Ye, L.A. Baker, Nano Lett. 20 (2020) 1233–1239.
[53] A. Hamelin, J. Electroanal. Chem. 407 (1996) 1–11.
[54] W. Chen, J. Xue, Y. Bao, L. Feng, Chem. Eng. J. 381 (2020) 122752.
[55] Z. Chen, C.X. Kronawitter, B.E. Koel, Phys. Chem. Chem. Phys. 17 (2015) 29387–29393.
[56] Y. Tian, H. Liu, G. Zhao, T. Tatsuma, J. Phys. Chem. B 110 (2006) 23478–23481.
[57] S. Wang, J. Zhang, O. Gharbi, V. Vivier, M. Gao, M.E. Orazem, Nat. Rev. Methods Prim. 1 (2021) 1–21.
[58] T.-N. Chen, J.-C. Kao, X.-Y. Zhong, S.-J. Chan, A.S. Patra, Y.-C. Lo, M.H. Huang, ACS Cent. Sci. 6 (2020) 984–994.
[59] C.-Y. Chu, M.H. Huang, J. Mater. Chem. A 5 (2017) 15116–15123.
[60] W.-C. Huang, L.-M. Lyu, Y.-C. Yang, M.H. Huang, J. Am. Chem. Soc. 134 (2012) 1261–1267.
[61] S. Sun, X. Zhang, Q. Yang, S. Liang, X. Zhang, Z. Yang, Prog. Mater. Sci. 96 (2018) 111–173.
[62] H. Zhuang, A.J. Tkalych, E.A. Carter, J. Phys. Chem. C. 120 (2016) 23698–23706.